



## Research papers

## Field observation and micro-mechanism of roots-induced preferential flow by infiltration experiment and phase-field method

Jiaying Li <sup>a,c</sup>, Peng Cui <sup>a,c,\*</sup>, Yanzhou Yin <sup>b</sup><sup>a</sup> Key Laboratory of Mountain Hazards and Earth Surface Processes, Institute of Mountain Hazards and Environment, Chinese Academy of Sciences (CAS), Chengdu 610041, China<sup>b</sup> State Key Laboratory of Hydroscience and Engineering, Tsinghua University, Beijing 100084, China<sup>c</sup> University of Chinese Academy of Sciences, Beijing 100084, China

## ARTICLE INFO

## ABSTRACT

## Keywords:

Root-Soil-Water System  
Preferential Flow  
Root Density  
Dye Tracer  
Phase-Field Method

Plant roots potentially contribute to slope instability by causing infiltrating water to be spatially and temporally redistributed in the soil unevenly following rainfall. But the root system's macro-scale impact on water infiltration and the formation and dynamics of pore-scale preferential flow induced by roots are still ambiguous. A field dye infiltration experiment was used to simulate rainwater infiltrating into the soil to quantify the relationship between preferential flow pathways and root characteristics such as root density and root number. A two-dimensional phase-field model was used to describe quantificationally and visually the influence of fluid pressure difference, wall contact angle, and pore throat size on vapor–liquid interface movement in the root-particle and interparticle pores. Water flows more freely along an extension direction of shallow coarse-root (diameter > 5 mm), facilitating water transfer between adjacent profiles. The dye coverage and preferential flow fraction are found to be significantly positively correlated with the fine-root (diameter < 5 mm) density and the coarse-root quantity. At the pore scale, a low difference of fluid pressure exerts more control from the root system over preferential flow, especially, the vapor–liquid interface in the root-particle pore lowers to the pore outlet about 50 % faster than the inter-particle pore for no pressure difference. The larger wall contact angle of the particle causes a more pronounced lowering rate of the vapor–liquid interface. With smaller pores, the flow rate accelerates. Smaller pores make it harder for water to flow from the interparticle pores than root-particle pores. Our findings can help to more accurately determine the depth of water infiltration in the slope and deeply understand the physical mechanism of the effect of the root system on rainwater redistribution.

## 1. Introduction

Shallow landslides caused by rainfall usually occur in mountainous areas such as southern China and parts of south-central and southwestern China after intensive or prolonged rainy seasons (Chen and Lee, 2003). Numerous investigations have demonstrated that plant-covered slopes differ mechanically and hydrologically from bare slopes, and hydrological processes have a more significant impact on vegetation slope stability (Wu et al., 1979). The roots, as a key component linking the plant to the soil, have a profound impact on hydrological processes in forested environments, in addition to the soil structure (Sidle and Bogaard, 2016). The primary root systems can extend deep into the soil or bedrock, where they can transport water and

create a dangerous sliding surface due to an increase in pore water pressure (Balzano et al., 2019; Mulyono et al., 2018). Besides, the interface between a soil slope's root-rich and rootless zones is another possible location for the development of a sliding surface (Baker et al., 2021; Liu et al., 2016a).

Plant roots usually have a significant impact on water infiltration due to the inhomogeneity of pore space caused by root vital activities and root system interactions (Bodner et al., 2014; Weiler and Naef, 2003; Wu et al., 2022). Roots generally improve soil permeability by wedging into weathered rocks and soils or decaying to form channels, which increases infiltration rates and fluxes during rainfall infiltration (Cui et al., 2022; Freer, 1991; Luo et al., 2019). On the other hand, roots can reduce soil permeability, a process that is most prevalent in the earliest stages of

\* Corresponding author at: Key Laboratory of Mountain Hazards and Earth Surface Processes, Institute of Mountain Hazards and Environment, Chinese Academy of Sciences (CAS), Chengdu 610041, China.

E-mail address: [pengcui@imde.ac.cn](mailto:pengcui@imde.ac.cn) (P. Cui).

root growth and under conditions of high soil porosity (Markart et al., 2011; Singh et al., 2018). Previous statistical results indicated that the percentage change in soil saturation infiltration rate caused by tree and shrub roots ranged from -140 % to 109 % and that the corresponding value for herbaceous roots ranged from -90 % to 650 % (Lu et al., 2020). Therefore, broad statements about the effect of plant roots on permeability are inappropriate because it depends greatly on soil and root type.

One of the main reasons roots promote water infiltration is the preferential flow formed by the root system (Levia and Frost, 2003; Schwärzel et al., 2012). Preferential flow, in contrast to matrix flow, always describes the irregular and frequently rapid movement of water and solutes around the soil matrix via the macro pores network (Allaire et al., 2009; Hendrickx and Flury, 2001). Pore continuity (Booltink and Bouma, 1991) and pore density (Smettem, 1986) are all factors that affect preferential flow. While the distinctive structural features of the root system and the interactions between roots lead to the formation of pore channels with widespread distribution, stability, and continuity, and are therefore particularly important in preferential flow study. Therefore, water may preferentially move through soil profiles that have a lot of roots (Luo et al., 2019). Many roots make a network of channels that facilitate rapid lateral water movement through the soil (Levia and Frost, 2003; Schwärzel et al., 2012). Devitt and Smith (2002) found that macro pore channels created by shrub roots in dry areas improved water flow downwards in desert soils, and the more roots there are, the stronger the preferential flow. Similarly, Song et al. (2017) found that the formation of preferential flow routes by vetiver grasses with main root systems may have improved unsaturated infiltration rates.

The influence of root systems on preferential flow is significantly related to the root diameter ( $d_r$ ) and its arrangement. There is some evidence that fine ( $d_r < 5$  mm) and coarse roots ( $d_r > 5$  mm) all aid water movement, but their mechanisms of action are distinct (Bodner et al., 2014). Together with surface microorganisms, fine roots release polysaccharides and other chemicals that aggregate clay particles that contribute to enhancing the stability of soil aggregates which increases the soil's permeability and infiltration rate (Paterson et al., 2007; Tisdall and Oades, 2006; Erktan et al., 2015; Vannoppen et al., 2015). Many fine roots can grow close together and even tangle with one another to form a complex root network that promotes water flow (Löbmann et al., 2020). While the coarse roots may be more efficient at transporting water between soil layers because of their longer length compared to fine roots (Martinez et al., 2021). Furthermore, some root shrinks during growth to create a circular gap that makes it easier for water to flow (Ghestem et al., 2011). To date, the phenomenon of preferential flow induced by root systems has been observed frequently, and the relative macro contributing factors and the mechanism of triggering landslides have been elucidated. However, the physical process of pore-scale root-induced preferential flow is not clear, which limits us to the understanding of the action mechanism of macro factors on preferential flow.

Insight into hydrological processes under the control of plant roots can be gained by analyzing the root-soil moisture distribution both spatially and temporally. Dye tracing is the most widely used technique for visualizing water flow because it allows observation of the water flow route without disturbing the soil. Analyzing the image after dyeing provides a semi-quantitative assessment of the flow state (Flury and Flühler, 1995). Dyed areas have traditionally been evaluated quantitatively using parameters like preferential flow fraction (Pr-fr) and length index (Bargues Tobella et al., 2014; van Schaik, 2009). We use the dye tracing method to visualize the preferential flow pattern of soil, analyze the dyeing ratio of roots, regional root density, and dyeing parameters to conclude the relationship between root characteristics and preferential flow, and thus gain a better understanding of the temporal and spatial distribution of water in the root-soil system.

Root-induced preferential flow is a process involving the transport of vapor–liquid interface along the solid pore walls and is related closely to the multiphase flow motion process. Our in-depth analysis of root-

induced preferential flow is limited by the dye experiment's ability to only produce the results of the final spatial distribution and not to track the progress of the fluid movement in the pore space over time. As a result, we simulate the multiphase flow transport mechanism within the pore medium and the pore space between the roots and soil using the phase-field method. The phase-field method can more naturally follow the evolution of a complicated free surface, and it is more accurate in terms of pressure gradients and velocity profiles than other interface tracking methods like the level set method and the volume-of-fluid method (Xiao et al., 2019). To better understand the mechanism of macroscopic root action on preferential flow at the microscopic level, we use the phase-field method to obtain the interfacial variation patterns of water–air two-phase flow under different simplified models, pore throat sizes, and inlet pressure conditions, thus explaining the observed phenomena in the field.

In this study, we chose a typical distribution of coniferous forests in the hilly region of southwest China as the study area. To quantitatively describe the influence of the root system on preferential flow, we conducted an experiment using the Brilliant Blue FCF tracer to investigate the characteristics of root-soil water flow affected by the root system. The results of numerical simulations are further combined with the results of the field scale to explain why the root system promotes preferential flow. Finally, the mechanism of the root-induced preferential flow is explained together at the pore scale and the field scale.

## 2. Materials and method

### 2.1. Field experiment

#### 2.1.1. Experimental site

A field experiment was performed in the Longchi National Forest Park (31°8'10"W, 103°34'32"E), located northwest of Chengdu in Sichuan Province, China. The climate in the study area is humid subtropical monsoon, with four distinct seasons (Zhang et al., 2021). The average annual temperature is 15.2 °C, and the average annual rainfall is roughly 1300–1450 mm (Jiang et al., 2022). Rainfall occurs frequently and heavily during summer, with 70 % of it falling between June and September. The bedrock in the study area mainly consists of granite, amphibolite, and Triassic rocks, with a general thickness of 50–130 cm of soil over bedrock and a humic layer thickness of about 1–1.3 cm (Mehtab et al., 2020; Stokes et al., 2007). Coniferous and broad-leaved mixed forest is the main vegetation type in the Longxi River Basin. No precipitation fell during our experiment in June.

We choose a well-developed root system and gently sloping site surrounded by four firs with an average height of 20 m. Three ring knives were used to measure the dry density and natural moisture content at different depths, in the ranges of 0–20 cm, 20–40 cm, and 40–60 cm. The physical parameters of the soils are shown in Table 1. The soil is found to be sandy loam in the depth range of 0–60 cm, indicating a large sand content at the sample site (USDA-NRCS, 1997). The dry density in the range of 0–20 cm soil layer is the largest and the initial moisture content of the soil is also the largest, reaching 36.86 %.

#### 2.1.2. Dye experiment

A square steel frame (120 cm × 120 cm) was vertically pushed into

**Table 1**  
Soil physical properties.

Soil physical properties	Depth (cm)		
	0–20	20–40	40–60
Soil density (g/cm <sup>3</sup> )	1.482	1.460	1.436
Initial moisture content (%)	36.86	30.36	27.58
Sand content (%)	86.4	70.2	68.5
Silt content (%)	9.5	23.9	23.7
Clay content (%)	4.1	5.9	7.8

the soil at a depth of 10 cm and the steel wall's 10 cm high aboveground section served as a barrier to prevent the dye tracers from escaping the frame (Fig. 1). The ground was compacted both on the inside and the outside of the steel wall near the edge, and fresh litter was removed from within the frame without damaging the humus layer on the surface. We picked Brilliant Blue FCF for this experiment due to its great visibility and low toxicity, and set the dye solution concentration to 4 g/L (Flury and Flühler, 1995). The 87 L of dye solution (equal to 6 cm rainfall) was sprayed uniformly. To avoid rain and evaporation, the whole frame was then covered with a piece of canvas.

After 24 h, the canvas and steel frame were gently removed. After that, the profiles were dug to a depth of 60 cm, depending on the depth of soil dyeing and the position of bedrock. To avoid boundary effect, we collected the soil profiles starting at 10 cm from one steel frame's edge with a lateral increment of 10 cm in the horizon ( $D_y$ ) and width ( $D_x$ ) direction, and eventually produced a sample plot of 100 cm × 100 cm. Then, each vertical portion was trimmed with a soil cutter after excavation. Following that, a vertical plane of  $D_x = 100$  cm and  $D_z = 60$  cm was shot and geometric distortion was adjusted using the ruler's edge points.

Because the tracer experiment lasted 24 h, root absorption also had an impact on water redistribution in the soil (Wang et al., 2015). According to the data in the Famine Early Warning Systems Network Land Data Assimilation System, none of the daily average transpiration during the experiment surpassed 3 mm, which was considerably less than infiltration (Amy McNally NASA/GSFC/HSL, 2018). So we ignored the influence of transpiration here.

### 2.1.3. Image analysis

Perform geometric correction on the obtained dyed image. To distinguish more precisely between dyed and undyed areas of the soil profile, we used the "Trainable Weka Segmentation" module of the software image J to classify the soil within the obtained photographs (Lormand et al., 2018). The same post-training categorization rules were then applied to all profile photographs. The obtained image was binarized, and the dye region was represented by black.

To characterize the dye path in the soil vertical profile, dye coverage (DC) and Pr-fr introduced by van Schaik (2009) and Bargues Tobella et al. (2014) were used. DC (%) is the proportion of the dyed area to the sum of the dyed and undyed areas.

$$DC = \left( \frac{D}{D + ND} \right) \times 100\% \quad (1)$$

where  $D$  (cm<sup>2</sup>) and  $ND$  (cm<sup>2</sup>) are the dyed area and the undyed area, respectively. The DC is calculated according to the percentage of black pixels in each horizontal line in the binary images for each vertical profile.

Pr-fr(%) is the fraction of the total infiltration that flows along preferential flow pathways.

$$Pr-fr = \left( 1 - \frac{UniFr \cdot W}{TSA} \right) \times 100\% \quad (2)$$

where  $UniFr$  is the uniform infiltration depth (cm) that is defined as the depth at which the DC decreases below 80 %,  $W$  is the width of the vertical profile (100 cm), and  $TSA$  is the total dyed area (cm<sup>2</sup>).

### 2.1.4. Root sample collection and quantification

The Brilliant Blue dyes the root surface after the dye tracer runs through the root channel, therefore it is reasonable to conclude that root dyeing is caused mostly by the preferential flow path. A total of ten soil blocks (100 cm × 10 cm × 60 cm) between two vertical profiles ( $D_y = 10$  cm) was brought back intact in cling bags. All roots picked from the soil and brought back to the lab were examined under natural light to determine whether they had been dyed or left undyed (Luo et al., 2018). In contrast to undyed roots, most dyed roots have 80–90 % or more of their total root surface area dyed. Then, using a vernier caliper, we measured all of the collected roots and divided them into six groups with dyed and undyed roots based on their diameters. Soak the roots in water to remove attached soil particles without destroying their structure. Then, the root was put in an oven at 65 °C (Zhang et al., 2012). After 24 h, the root was taken out and weighed, which was the dry weight of the roots ( $W_d$ ).

Root area density (RAD) and root mass density (RMD) are used to quantify the root density of different soil layers (Mehtab et al., 2020; Zhang et al., 2012). RAD is defined as the ratio of the total cross-sectional area ( $S_r$ ) of plant roots to the total cross-sectional area ( $S_s$ ) of the soil.

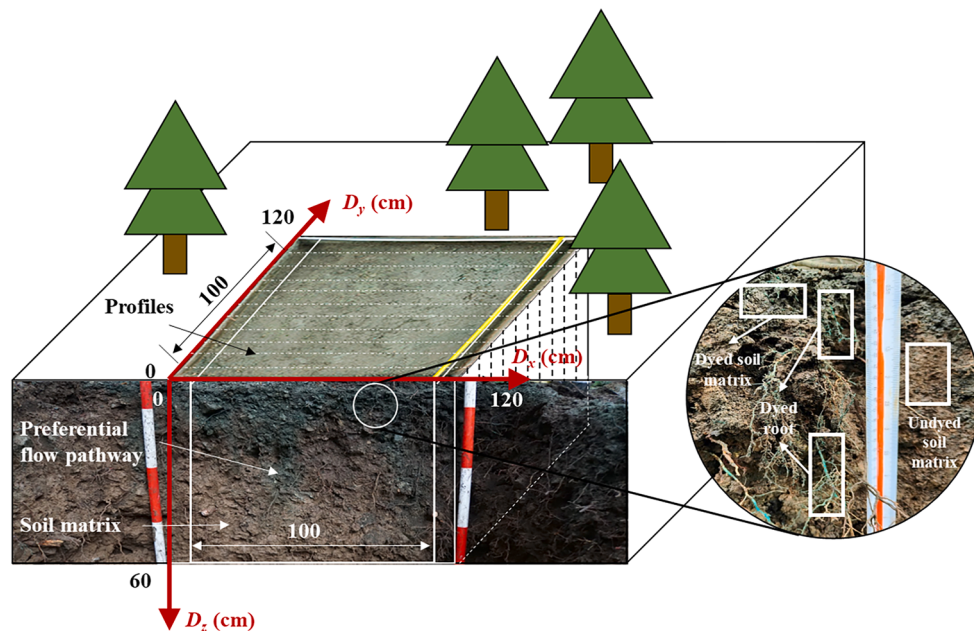


**Fig. 1.** Zone of the dye tracer experiments with size 120 cm × 120 cm × 60 cm and the size of soil sampling zone is 100 cm × 100 cm × 60 cm.

$$RAD = \frac{S_r}{S_s} \times 100\% \quad (3)$$

Also, *RMD* is the dry weight ( $W_d$ ) of roots per unit volume of soil ( $V_s$ ).

$$RMD = \frac{W_d}{V_s} \times 100\% \quad (4)$$

We utilized the 'measurement' tool of software image J to get the root coordinates and  $d_r$  of each piece. Only live roots were considered in the statistics. Finally, we obtained the root distribution and each layer's *RAD* of 11 profiles. The total *RAD* at different locations required for the calculation is the sum of the *RAD* extracted within the area of the region.

## 2.2. Numerical analysis

The phase-field method is used to track the interface of a two-phase flow (Bai et al., 2017). A Cahn-Hilliard equation (Cahn and Hilliard, 1958) governs the dynamics of a two-phase flow. The diffuse interface is defined as the region where the dimensionless phase field variable  $\phi$  goes from -1 to 1. The Cahn-Hilliard equation is expressed as follows:

$$\frac{\partial \phi}{\partial t} + u \bullet \nabla \phi = \nabla \bullet \frac{\gamma \lambda}{\epsilon^2} \nabla \psi \quad (5)$$

$$\psi = -\nabla \bullet \epsilon^2 \nabla \phi + (\phi^2 - 1)\phi + \left(\frac{\epsilon^2}{\lambda}\right) \frac{\partial f_{ext}}{\partial \phi} \quad (6)$$

where  $u$  is the fluid velocity field,  $t$  is time,  $\gamma$  is the mobility parameter,  $\psi$  is an auxiliary variable (Qin and Bhadeshia, 2013),  $\lambda$  is the mixing energy density, and  $\epsilon$  is a control parameter for the interface thickness that scales with a thickness of the interface (Qian et al., 2005). We set  $\epsilon = h_c/2$ , where  $h_c$  is the characteristic mesh size in the region passed by the interface. The parameters  $\lambda$  and  $\epsilon$  are related to interfacial tension  $\sigma$ .  $f_{ext}$  is an external force due to the free energy, and  $f_{ext} = 0$  in this work. We define air as fluid 1 ( $\phi = -1$ ) and water as fluid 2 ( $\phi = 1$ ), while it changes in (-1, 1) at the air-water mixing zone. The volume fraction of both is expressed as follows:

$$V_{f1} = \frac{1 - \phi}{2} \quad (7)$$

$$V_{f2} = \frac{1 + \phi}{2} \quad (8)$$

The multi-physics coupling feature defines the density  $\rho$  and the viscosity  $\mu$  of the mixture to vary smoothly over the interface by letting

$$\rho = \rho_w + (\rho_{air} - \rho_w)V_{f2} \quad (9)$$

$$\mu = \mu_w + (\mu_{air} - \mu_w)V_{f2} \quad (10)$$

where the water and air properties are denoted *w* and *air* respectively. The mass and momentum transfer of the fluid is modeled based on the Navier-Stokes equation for incompressible fluids (Jacqmin, 1999). Also, the effect of surface tension is considered in the model. Thus, the N-S equation is expressed as:

$$\rho \frac{\partial u}{\partial t} + \rho(u \bullet \nabla)u = \nabla \bullet [-pI + \mu(\nabla u + (\nabla u)^T)] + F_{st} + \rho g \quad (11)$$

$$\nabla \bullet u = 0 \quad (12)$$

where  $p$  denotes the pressure,  $I$  is the unit tensor and  $g$  is the gravity vector.  $F_{st}$  is the surface tension force acting at the air/water interface.

$$F_{st} = G\nabla\phi \quad (13)$$

where  $\phi$  is the phase field parameter,  $G$  is the chemical potential:

$$G = \lambda \left[ -\nabla^2\phi + \frac{\phi(\phi^2 - 1)}{\epsilon^2} \right] \quad (14)$$

Scanlan (2009) assumed that the geometry of roots within pore space can be represented by concentric cylinders to study root-induced changes to soil hydraulic properties. However, the pores between particles and roots are undulated (Lei et al., 2021). They control the flow of water, directing it to go through pores in whichever direction has the lowest capillary pressure threshold (Lu et al., 2019). Therefore, as shown in Fig. 2 (b), we used a simplified model of the root-soil system in which the root is represented by cylinders and the soil particles by balls in this simulation. The pores can be simplified to the root-to-particle (RP) model (Fig. 2 (a)) and the particle-to-particle (PP) model (Fig. 2 (c)) in the two-dimensional (2D) cross-section of the root-soil system.

In this simulation, we assume that water and air are incompressible, and the gravity direction is set to coincide with the water flow direction to simulate the vertical infiltration process. Both inlet and outlet are pressure boundaries. The density and viscosity of air and water are the standard values at 24 °C (Table 2). As we consider the comparison of different situations, higher mobility is used in this study to obtain the correct pressure change at the interface. Other parameter values are shown in Table 2. The particle radius is set to 0.1 mm because the size of the particle with high content is 0.02-2 mm in the experimental sample site (Table 1).

The contact angle measures the ability of a liquid to wet a solid surface (Jang et al., 2016). Therefore, the contact angle must take into account the difference between the root wall and the particle wall. The corresponding contact angles of 87° for subgrade soil and 58° for silica sand are obtained based on the curve of contact angle versus particle size obtained experimentally by Liu et al. (2016b). In the PP model, the contact angle of the particle wall ( $\theta_p$ ) is the same on both sides, and  $\theta_p = 87^\circ$  or 58°. In the RP model,  $\theta_p = 87^\circ$  or 58° and the contact angle  $\theta_r$  of the root wall is 67.5° according to the measured value (Ahmed et al., 2016b; Hauber et al., 2020). Since the pore diameter is 0.155 times the particle size when the particles are closely packed and 0.414 times the particle size when they are loosely packed (Riha et al., 2018), the pore diameters of the two corresponding packing states in the experiment should be less than 0.31 and 0.82 mm, respectively. For this, we choose pore throat sizes ( $d_c$ ) of 0.02, 0.05, 0.08, and 0.1 mm to run independent simulations. Finally, the water depth,  $\rho_w$ , and  $g$  can be used to figure out the pressure per unit area. For the dye infiltration experiment, the head height was 6 cm, so the pressure at the surface was 600 Pa. As the depth of the soil layer increased, the head pressure at the entry gradually decreased until 0 Pa. Therefore, the pressure difference ( $\Delta p$ ) of 0, 200, 400, and 600 Pa (equal to the height of the water head of 0, 2, 4, and 6 cm) are set to characterize the infiltration conditions for different soil depths after the outlet pressure is set to 0 Pa. Table 3 displays the specific settings for each of the 28 sets of simulation experiments.

## 3. Results

### 3.1. Dye infiltration experiment

#### 3.1.1. Features of roots in soil layers

The *RAD* of fine roots in the 11 profiles tends to fall with depth. While the *RAD* of coarse roots is largest at  $D_y = 10 - 20$  cm and tends to fall with depth (Fig. 3 (a)). As shown in Fig. 3 (b), the *RAD* of fine roots is the largest at  $D_y = 70$  cm, which corresponds to the vegetation distribution of the sample site. Meanwhile, the fine root density is larger at  $D_y = 0 - 70$  cm and the coarse root density is higher at  $D_y = 80 - 110$  cm, suggesting that there is a dividing line of root density of coarse and fine root located at  $D_y = 70 - 80$  cm.

We use the ratio  $RMD_d/RMD_n$  ( $RMD_d$ : the *RMD* of dyed roots,  $RMD_n$ : the *RMD* of undyed roots.) to determine the degree of root dyeing. It can indicate the degree of water flow along roots of varying diameters as

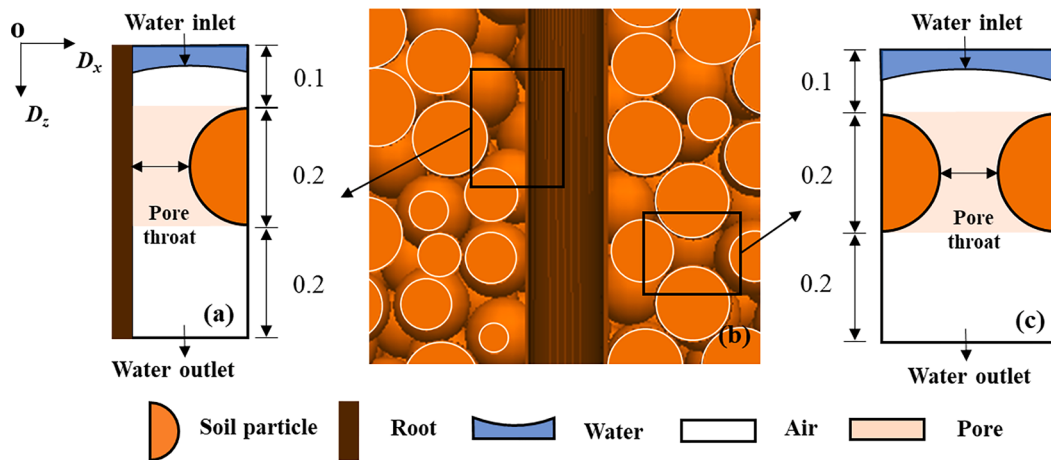


**Fig. 2.** Simplified model. (a) 2D root-to-particle (RP) model, (b) 3D cylindrical root-ball model, (c) 2D particle-to-particle (PP) model. Unit is mm.

**Table 2**  
Parameters set in the simulation.

Parameter	Value	Description
$\rho_w$ (kg/cm <sup>3</sup> )	$1.0 \times 10^3$	Density of water
$\rho_{air}$ (kg/cm <sup>3</sup> )	1.29	Density of air
$\mu_w$ (Pa·s)	$1.01 \times 10^{-3}$	Viscosity of water
$\mu_{air}$ (Pa·s)	$17.90 \times 10^{-6}$	Viscosity of air
$\gamma$ (m·s/kg)	30.0	Mobility parameter
$g$ (m/s <sup>2</sup> )	9.8	Gravitational acceleration
$\epsilon$ (m)	$4.0 \times 10^{-4}$	Control parameter for the interface thickness

shown in Fig. 4. This ratio between 0 and 1 suggests a greater mass of undyed roots, whereas a ratio greater than 1 indicates a larger mass of dyed roots. According to the results of  $RMD_d/RMD_n$  versus  $d_r$  for 10 root-soil blocks, the ratio of dyed to undyed roots drops as  $d_r$  increases (Fig. 4). For  $d_r > 5$  mm, more mass of undyed roots exists in 75 % of 10 root-soil blocks than dyed roots. For roots with  $2 \text{ mm} < d_r < 5$  mm, 70 % to 75 % of 10 root-soil blocks have more dyed roots than undyed roots. While in all zones of the area, the mass of dyed roots is larger than the mass of undyed roots for roots with  $d_r < 2$  mm. From the experiments, finer roots appear to influence water infiltration more than coarser roots.

**Table 3**  
Selection of variables in the simulation.

Model	Particle contact angle $\theta_p$ (°)	Root contact angle $\theta_r$ (°)	Pressure difference $\Delta p$ (Pa)	Pore throat size $d_c$ (mm)
RP model	58	67.5	0, 200, 400, 600	0.1
	87		0	0.02, 0.05, 0.08
	58	–	0, 200, 400, 600	0.1
	87		0	0.02, 0.05, 0.08
PP model	58	–	0, 200, 400, 600	0.1
	87		0	0.02, 0.05, 0.08
	58	–	0, 200, 400, 600	0.1
	87		0	0.02, 0.05, 0.08

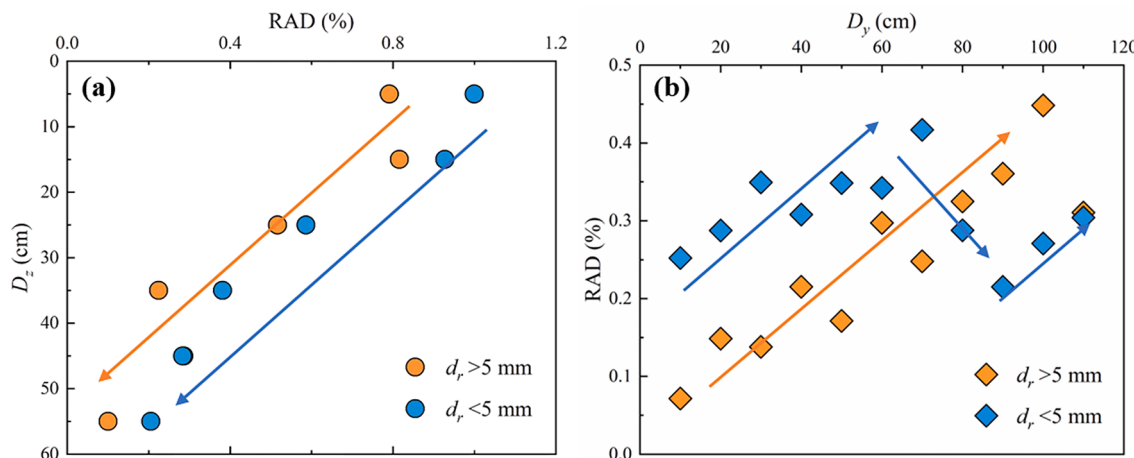


**Fig. 3.** Root distribution of the plot. (a) The changes of RAD with different  $d_r$  in each layer (10 cm) in the  $D_z$  the direction of 11 profiles, (b) the trend of the change of RAD with different  $d_r$  in the  $D_y$  the direction of the profile.

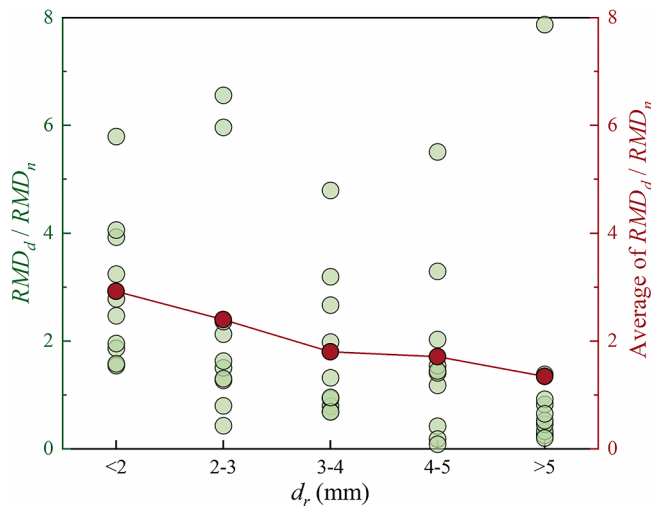


**Fig. 4.**  $RMD_d / RMD_n$  versus  $d_r$  for eleven profiles.  $RMD_d$  is the  $RMD$  of dyed roots and  $RMD_n$  is the  $RMD$  of undyed roots.

### 3.1.2. Dyeing indexes for soil profiles

It is discovered that DC increases to 100 % in the depth range of 0-5 cm, then decreases with the increase of  $D_z$  shown from the photographs in Fig. 5 (d-f). We classify the 11 datasets into three types, each showing a distinct pattern of dyeing between 0-20 cm and 20-40 cm in the  $D_z$  direction. The first type is characterized by uniformly shallow infiltration for  $D_y = 30, 40, 60$  cm (Fig. 5 (a) and (d)). At  $D_z = 0-20$  cm, the DC for this type has an exponentially decreasing trend, and it is already less than 20 % with essentially no DC at  $D_z = 20-60$  cm. The second type is non-uniformly shallow infiltration for  $D_y = 50, 80, 90, 100, 110$  cm (Fig. 5 (b) and (e)). This type of DC displays a linear decrease from  $D_z = 5-40$  cm, no DC from  $D_z = 40-60$  cm, and non-uniform localized dyeing. Deep infiltration is the third type for  $D_y = 10, 20, 70$  cm (Fig. 5 (c) and (f)). At  $D_z = 0-60$  cm, the DC of this type shows a linearly decreasing trend, and at  $D_z = 20$  cm, it might still approach 50 %.

Table 4 displays the additional parameters for the 11 profiles at 10-110 cm in the  $D_y$  direction, including total DC, maximum dye depth ( $DD_{max}$ ), DC per layer, and Pr-fr. It can be seen that the change in DC every 10 cm is consistent at  $D_z = 20-60$  cm. The trend of DC fluctuation in every 10 cm depth range was the same for the 11 profiles. However, when  $D_y = 10-20, 50-70, 100-110$  cm, the fluctuation trend of DC is opposite at  $D_z = 0-10$  cm and  $D_z = 10-20$  cm.

### 3.1.3. Root-soil and dyeing indexes of soil profiles

The uniformly shallow infiltration ( $D_y = 40$  cm) displays the highest decrease in fine roots and coarse roots density at  $D_z = 0-20$  cm, which leads to the lowest RAD of coarse roots at  $D_z = 20$  cm (Fig. 5 (g)). Correspondingly, it has the largest DC drop of 40%, indicating an inadequate hydrological connection in shallow soil layers with consistently weak infiltration. While non-uniformly shallow infiltration (Fig. 5 (h)) and deep infiltration (Fig. 5 (i)) contain high RAD of both coarse and fine roots, even the root density is increasing, leading to less amount of DC decline in the shallow layer. At  $D_z = 20-40$  cm, the RAD of coarse and fine roots is larger for deep infiltration, while the DC is higher and the dye solution is easy to enter (Fig. 5 (i)). While for both uniformly and non-uniformly shallow infiltration, the RAD of the roots is reduced by 60 % at  $D_z = 20-40$  cm and DC drops to 0. This indicates that the larger the root density, the greater the soil hydrological connectivity.

The correlation between root parameters and DC is proved based on the relationship between root density and DC in the above typical profiles. We use the DC per 10 cm soil layer in the  $D_y$  direction for each profile as the dependent variable and the root system indicators, such as

$RAD$  and root number ( $N_r$ ) as the independent variables (Table 5). The correlation coefficients for fine roots are 0.834 between  $RAD$  and DC and 0.816 between  $N_r$  and DC. It is significant at the 0.01 level, indicating a strong positive correlation between the density of fine roots and DC. Similarly, there is a positive correlation between the density of coarse roots and DC, while the  $N_r$  of coarse roots is more strongly associated with DC. It indicates that the DC in each layer decreases as the  $RAD$  or  $N_r$  of the plant roots decrease.

To investigate the association between preferential flow parameters and root parameters, a statistical analysis of the Pr-fr and the  $N_r$ ,  $RAD$  of each diameter in 11 profiles is conducted. According to Table 6, the root indexes with  $2 \text{ mm} < d_r < 3 \text{ mm}$  has correlation coefficient values greater than 0.7 with Pr-fr ( $p < 0.01$ ), and the root indexes with  $d_r < 2 \text{ mm}$  has correlation coefficient values greater than 0.6 with Pr-fr ( $p < 0.05$ ), indicating a strong positive correlation between fine roots and Pr-fr. While the root indexes with  $4 \text{ mm} < d_r < 5 \text{ mm}$  shows a strong negative correlation with Pr-fr ( $p < 0.05$ ) and the root indexes with  $d_r < 5 \text{ mm}$  has a weak negative correlation with Pr-fr. It indicates that the Pr-fr could increase as the  $RAD$  or  $N_r$  of the roots increases (for  $d_r < 3 \text{ mm}$ ) or the roots decrease (for  $d_r > 4 \text{ mm}$ ). It means that numerous fine roots enable better water flow than the coarse roots of the same  $RAD$ .

## 3.2. Movement of pore fluid for the RP and PP model

### 3.2.1. Fluid movement process

There are a total of 28 sets of simulation results for three parameters: the wall contact angle, the pressure difference, and the size of the  $d_c$ . The fluid movement of 28 simulations is discussed to reveal the physical micro-mechanism of the root-induced preferential flow that lies behind the experimental phenomenon of dye infiltration.

Only 17 of the 28 outcomes enable fluid to pass through to the outlet. The results of two models with  $\theta_p = 87^\circ$ ,  $d_c = 0.1 \text{ mm}$  and  $\Delta p = 200 \text{ Pa}$  are presented to illustrate two different overall infiltration processes seen in Fig. 6 (a) and (b). Clearly, water can flow out of the RP model in the same amount of time quicker. In the RP model, the liquid surface lowers along the root wall into the pore because  $\theta_r < \theta_p$  and it continues to lower along the root wall to the outlet (Fig. 6 (a)). In contrast, the PP model shows a convex liquid surface and then falls back. The particles on either side of the wall condition are identical, hence the lowering of the liquid surface is axisymmetric (Fig. 6 (b)). In both models, the surface tension of the liquid before the water reaches the pore throat is down, and after water flows through the pore throat, it is up. In Fig. 6 (a), the total  $\Delta p$  and gravitational force of the liquid are greater than the capillary force, allowing water to flow to the outlet. However, the capillary force is bigger than the sum of the other two forces, so the liquid surface moves back toward the pore throat in Fig. 6 (b).

Based on this, we obtain the relationship between the ratio of the downward flow height of the liquid surface ( $D_z$ ) and the total height of the model ( $D_h$ ) and the ratio of time used for the downward flow of the liquid surface ( $t$ ) and the time step ( $\Delta t = 1 \times 10^{-5} \text{ s}$ ) at the two walls of the RP and PP models (Fig. 6 (c)). It shows that the height of the root wall of the RP model is higher than that of the particle wall during the water motion. Also, water eventually reaches the outlet along the particle wall of the RP model, but it takes twice as long as at the root wall. In contrast, the liquid surface at the wall of the PP model cannot reach the pore outlet. Meanwhile, the liquid surface lowering rate of the particle wall in the RP model is higher than that in the PP model due to the pulling of the root wall on the liquid. This shows that the root can help direct water flow.

### 3.2.2. Effect of parameters

The  $D_{max}$  identifies the point of the highest velocity of movement during the downward flow of the liquid surface. It can most obviously represent the contribution of root presence to the transport of water. We use the time taken for the fluid to reach  $D_{max}$  as the vertical coordinate to

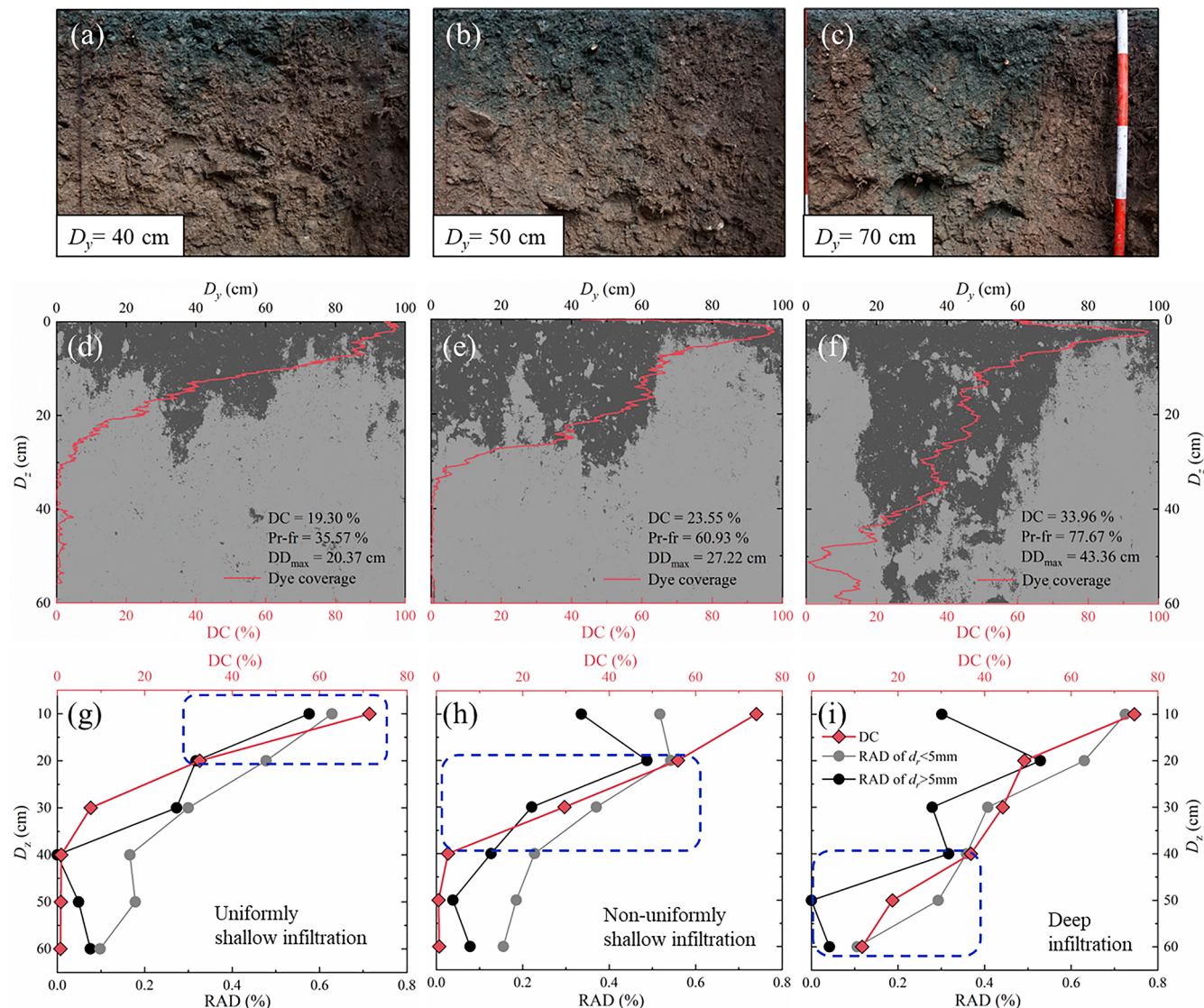


**Fig. 5.** (a)-(c) Dyed vertical soil profiles, (d)-(f) Image processing and analysis (where DC is dye coverage,  $DD_{max}$  is the maximum dyed depth, the red curve represents the change of dye coverage with depth), (g)-(i) RAD of coarse and fine roots and DC changes with  $D_z$  and  $D_y$  (where the dashed boxes represent the main root density difference between infiltration patterns). (For interpretation of the references to color in this figure legend, the reader is referred to the web version of this article.)

**Table 4**  
Dyeing indexes of soil profiles.

$D_y$ (cm)	DC (%)	$DD_{max}$ (cm)	DC in layer (%)						Pr-fr (%)
			0–10	10–20	20–30	30–40	40–50	50–60	
10	33.00	34.74	80.96	53.89	38.23	26.42	20.60	8.93	69.1
20	33.74	34.88	68.24	57.55	46.90	26.36	22.26	12.94	73.96
30	24.94	22.95	58.86	17.50	6.58	3.23	4.52	6.50	60.1
40	19.30	20.37	71.42	32.58	7.63	0.91	0.82	0.71	35.57
50	23.55	27.22	74.02	55.91	29.67	2.71	0.51	0.67	60.93
60	22.31	21.44	84.81	47.73	13.04	6.85	3.04	0.31	21.19
70	33.96	43.36	74.59	49.19	44.23	36.86	18.72	11.71	77.67
80	36.37	30.53	81.55	60.44	36.26	23.02	17.19	10.12	53.94
90	22.02	26.40	68.88	43.50	26.07	8.52	0.92	0.38	50.42
100	29.96	32.92	85.53	59.65	30.89	15.04	2.27	4.28	44.37
110	29.58	27.05	82.09	66.48	29.67	18.19	4.61	2.32	41.40

Maximum dyed depth: the depth of DC falls to 20%.

quantify the effect of different factors on the preferential flow as shown in Fig. 7.

$\Delta p$  is used to describe the water head pressure on infiltration. For

$\theta_r < \theta_p$ , with the same  $d_c$ , the larger  $\Delta p$  is, the faster the rate of liquid surface lowering of RP and PP models (Fig. 7 (a)). For  $\Delta p > 400$  Pa, the time required to reach the pore outlet is comparable for both models.

**Table 5**

Analysis of the correlation between the DC and the root indexes.

Root index	$d_r$ (mm)	DC (%)
RAD	$d_r > 5$	0.532**
	$d_r < 5$	0.834**
$N_r$	$d_r > 5$	0.703**
	$d_r < 5$	0.816**

\*\* Correlation is significant at the 0.01 level (two-tailed).

**Table 6**

Analysis of the correlation between Pr-fr and root indexes.

Root index	$d_r$ (mm)	Pr-fr (%)
RAD	$d_r < 2$	0.639*
	$2 < d_r < 3$	0.749**
	$3 < d_r < 4$	-0.168
	$4 < d_r < 5$	-0.660*
	$d_r > 5$	-0.531
$N_r$	$d_r < 2$	0.649*
	$2 < d_r < 3$	0.789**
	$3 < d_r < 4$	-0.097
	$4 < d_r < 5$	-0.617*
	$d_r > 5$	-0.556

\*Correlation is significant at the 0.05 level (two-tailed).

\*\* Correlation is significant at the 0.01 level (two-tailed).

This indicates that the flow velocity of water in the root-soil pores and soil pores are similar for shallow soil with high surface accumulated water amounts, and the roots show less advantage and do not reflect a preferential flow tendency. By decreasing  $\Delta p$  from 400 Pa to 200 Pa, the RP model shows an 18 % increase in the time required to reach the pore outlet, while the PP model shows a 25 % increase. As  $\Delta p$  decreases to 0 Pa, the time to reach the pore outlet  $t_{max}$  increased by 46 % for the RP model and 153 % for the PP model. This indicates that as the water infiltrates deeper into the soil, water flows more easily and more rapidly through the root-soil pore than through the interparticle pore, so creating a preferential flow path.

Moreover,  $d_c$  is used to explore the rate of  $D_{max}$  lowering under different pore sizes under no head pressure conditions when  $\theta_r < \theta_p$ . It shows that the rate of  $D_{max}$  lowering decreases as  $d_c$  increases shown in Fig. 7 (b) at water reaches the pore inlet stage and water flows within the pore. The time required for  $D_{max}$  to reach the pore inlet in the PP model

is three times that of the RP model, and the time required to reach the pore outlet for the PP model is about twice that of the RP model. Moreover, the RP model has a higher  $D_{max}$  after liquid surface stabilization than the PP model. This indicates that the water moves faster along the root under capillary force and gravity, and it is easier to enter the next pore since the liquid surface can reach a higher height.

For  $\theta_r > \theta_p$ , the overall influence of  $\Delta p$  and  $d_c$  on  $D_{max}$  of the two models is similar as  $\theta_r < \theta_p$  during the water flows from the model inlet to the pore outlet (Fig. 7 (c) and (d)). The difference is that for  $\theta_r > \theta_p$ , the fluid reaches the pore outlet more easily for both RP and PP models due to the smaller contact angle of the particle wall. With the same  $D_{max}$  increase trend, it is found that the lowering rate of  $D_{max}$  for  $\theta_r > \theta_p$  is faster compared to  $\theta_r < \theta_p$ . The time consumed for  $D_{max}$  to reach the pore outlet is essentially the same for the RP and PP models under different  $\Delta p$  and  $d_c$ , but the lowering rate of the liquid surface out of the pore is faster for the RP model.

### 3.2.3. Analysis of root-soil pore

It shows that the liquid surface enters the pore along the wall with the smaller contact angle in Fig. 6. To investigate the role played by the root wall in the inflow of water into the pore, we calculate the liquid surface lowering rate ( $v$ ) of the root wall and particle wall of the RP model shown in Fig. 8.

$$v = \frac{D_{in} - D_{out}}{t_{in} - t_{out}} \quad (15)$$

where  $D_{in}$  denotes the height of the pore inlet ( $D_z/D_h = 0.2$ ),  $D_{out}$  denotes the height of the pore outlet ( $D_z/D_h = 0.6$ ),  $t_{in}$  is the time for water to reach the pore inlet and  $t_{out}$  is the time for water to reach the pore outlet.

There is a linear increase relationship between  $v$  and  $\Delta p$  at both borders, with a larger velocity increment at the root wall (Fig. 8 (a)). The  $v$  of the root wall is near twice that of the particle wall, and the maximum  $v$  can reach 2.2 times when the  $\theta_p$  is larger ( $\Delta p = 200$  Pa,  $d_c = 0.1$  mm). Moreover, the  $v$  of the root wall is almost over twice that of the particle wall when the  $\theta_p$  is larger, as low as 2.3 times at  $\Delta p = 400$  Pa and  $d_c = 0.1$  mm. The liquid lowering rate at both walls tends to increase exponentially with decreasing  $d_c$ , and the trend is more obvious on the root wall (Fig. 8 (b)). As  $d_c$  decreases, the  $v$  of both the root wall and particle wall converge to the same for larger  $\theta_p$ . While the  $v$  of both the root wall grows at a faster rate than the particle wall as  $d_c$  decreases

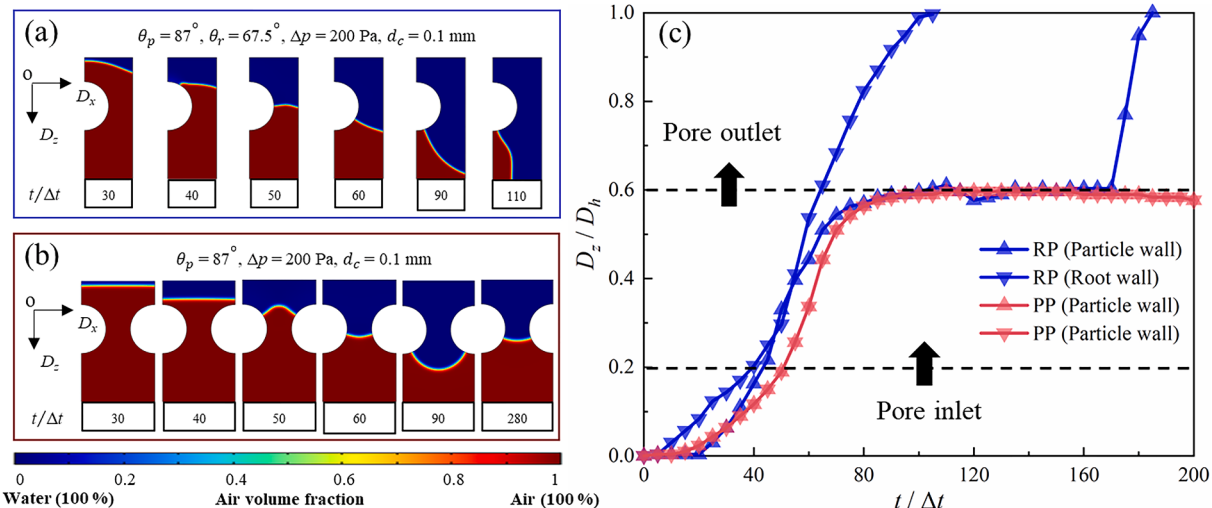


**Fig. 6.** (a) The liquid surface lowering of the RP model under  $d_c = 0.1$  mm,  $\Delta p = 200$  Pa,  $\theta_p = 87^\circ$ , (b) the liquid surface lowering of the PP model under  $d_c = 0.1$  mm,  $\Delta p = 200$  Pa,  $\theta_p = 87^\circ$ , (c) the liquid surface height changes with time along both walls of the two models. The bottom color line is air volume fraction, 0 is water and 1 is air.  $D_z$  is the downward flow height of the liquid surface,  $D_h$  is the total height of the model,  $t$  is the time of the downward flow of the liquid surface and  $\Delta t$  is the time step ( $1 \times 10^{-5}$  s).

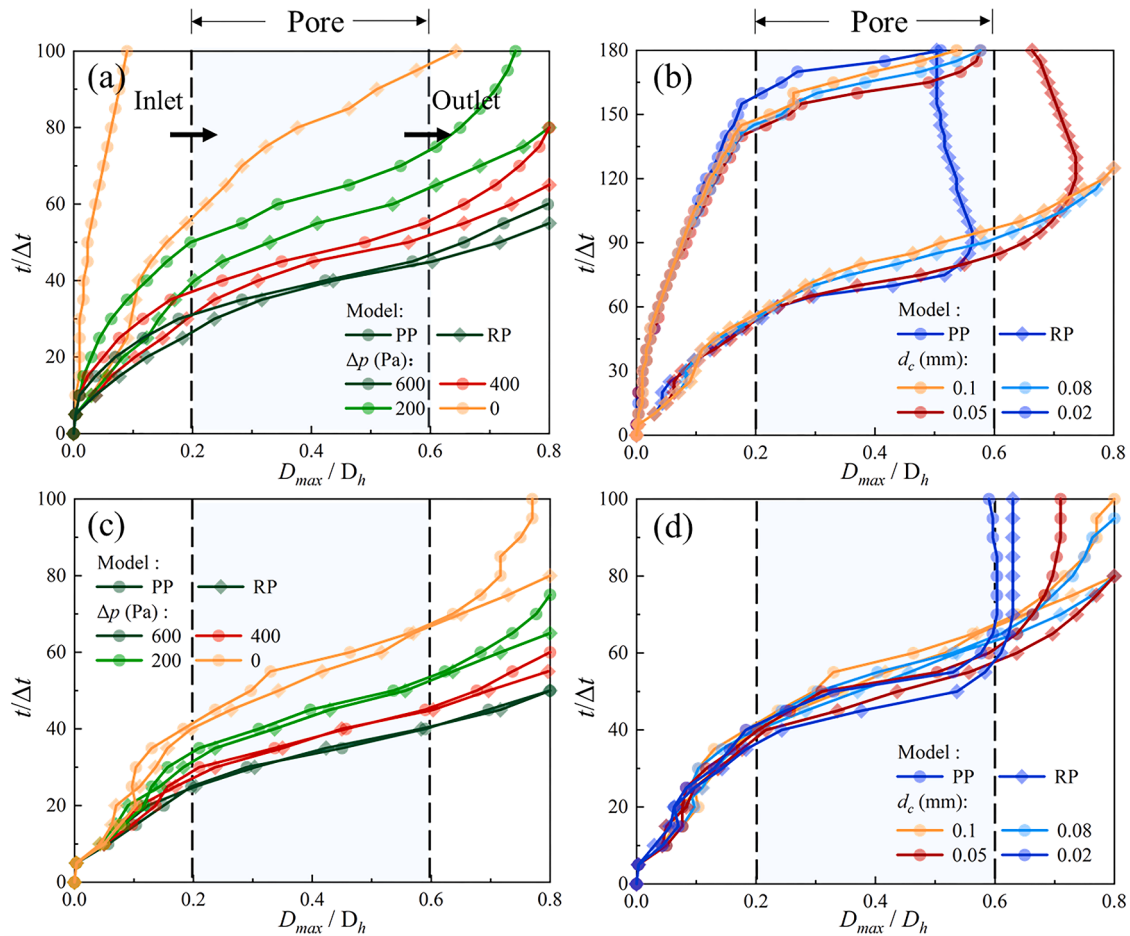


**Fig. 7.** The time consumed by the liquid surface lowering. (a)  $\theta_p = 87^\circ$ ,  $d_c = 0.1$  mm, (b)  $\theta_p = 87^\circ$ ,  $\Delta p = 0$  Pa, (c)  $\theta_p = 58^\circ$ ,  $d_c = 0.1$  mm, (d)  $\theta_p = 58^\circ$ ,  $\Delta p = 0$  Pa.  $D_{max}$  is the point of the highest velocity of movement,  $D_h$  is the total height of the model,  $t$  is the time of the downward flow of the liquid surface and  $\Delta t$  is the time step ( $1 \times 10^{-5}$  s).

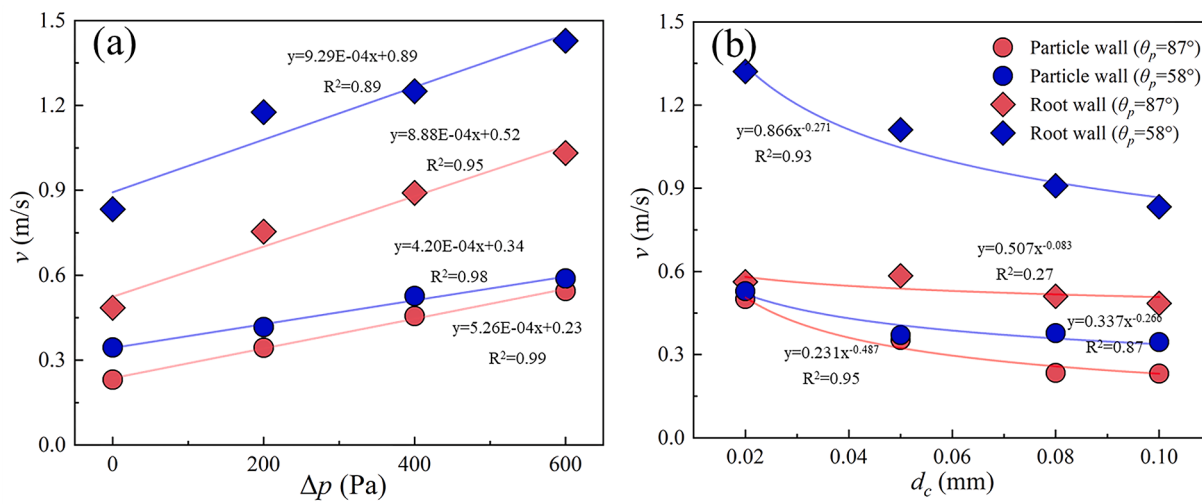


**Fig. 8.** Liquid surface raise rates within the pore for particle and root walls with (a)  $d_c = 0.1$  mm and (b)  $\Delta p = 0$  Pa.  $v$  is the flow rate of water in the pore.

for larger  $\theta_r$ . The maximum  $v$  at the root wall can be as high as three times the particle wall ( $\Delta p = 0$  Pa,  $d_c = 0.05$  mm). It showed that water moves more rapidly via the root-soil pore gap, facilitating faster entry of water to deeper soil layers along the roots.

#### 4. Discussion

##### 4.1. Effects of root density and diameter on preferential flow at the field scale

Under similar particle size distribution of the soil in each profile, the

dyeing patterns of each profile differ (Table 1, Table 4), suggesting that the root system plays a different role in infiltration (Wang et al., 2018). Consistent with the findings of Nobles et al. (2010) and Luo et al. (2019), the DC of the soil tends to decrease with depth (Table 4). The uniformity of the DC in the 0–5 cm deep range may correspond with the regional humus layer thickness (Mehtab et al., 2020). As the herbaceous vegetation on the surface layer has grown, the fine root development in the soil has become more homogeneous. The larger density and number of roots, as well as the complex root structure interspersed in the soil to generate numerous big pores with enhanced pore connection, are the key causes of the higher DC in shallow soil layers (Newman et al., 2004; Noguchi et al., 1997; Sidle et al., 2001; Jiang et al., 2021). Another explanation might be that biological activity decreases as soil depth increases, but exudates from microbes and plant roots can produce organic matter in the soil, and a larger organic matter concentration can aid vertical water transport (Ali et al., 2018). Root degradation also creates huge holes that function as preferential flow routes (Fageria and Stone, 2006; Ghestem et al., 2011). Therefore, as soil depth increases, the root density decreases, and so do hydrological connectivity and DC.

There is a positive correlation between coarse roots and dyeing indexes (Table 5). Coarse roots raised macro porosity by 30 % according to Bodner et al. (2014). Some scholars also point out that, the comparatively coarse and well-developed horizontal roots can aid in the lateral flow of water in the shallow layer, while the coarse roots that have grown vertically and the connected lateral roots can increase the longitudinal flow of water along the taproots (Cui et al., 2019; Fan et al., 2017; Ghestem et al., 2011). Consequently, it is also essential to consider how nearby soil profiles interact with one another. When water cannot infiltrate a profile below a deeper depth, it flows along the horizontal roots to the neighboring profiles by comparing the dyeing results by combining the results in Fig. 3 with Table 4. The root density decreased with soil depth, the less influence on the dyeing results of adjacent profiles. With high root density in the shallow layer, there was some mutual water feedback from adjacent profiles. However, the preferential flow index we obtained is not well related to the coarse root density, unlike the results of Dai et al. (2021). It may be since the characteristics of coarse roots cannot be fully characterized by two-dimensional cross-sectional area because coarse roots are longer, have a smaller specific surface area, and the RAD only weakly characterizes their conductivity. Due to the hot and humid climate of the study area, plant roots are shallowly developed and coarse roots are mostly distributed laterally (Jiang et al., 2022), which may also explain the weak correlation between coarse root density and preferential flow index.

Moreover, there is a significant correlation between fine roots and dyeing profile indexes (Table 5, Table 6). According to Bodner et al. (2014), fine roots cause pore space inhomogeneity and larger micro-pores volumes. They are easily twisted to form a complex root network, which increases the hydrological connectivity of the soil. Some study shows that fine roots affect aggregate stability (Hao et al., 2020). Fine roots have substantially higher root length densities and decomposability than coarse roots (Freschet et al., 2017). These enhance aggregate stabilization while improving soil porosity and reducing the clogging of loose clay particles in water channels (Bronick and Lal, 2005; Galloway et al., 2018; Ghestem et al., 2011). Meanwhile, under these climate and soil conditions, fine roots are shorter, more numerous, and have a large specific surface area. As a result, their RAD reflects their proportional contribution to preferential flow. Furthermore, there are many results on the effect of root density parameters on infiltration (Freschet et al., 2021), more indoor modeling studies are needed to confirm the precise effect of different root densities on infiltration.

Combining the previous analyses, it is possible to classify the infiltration patterns of the root-soil system. When there are more fine roots and the coarse roots are primarily developed horizontally, uniformly shallow infiltration will occur. The typical example is the water infiltration process in grassland and cropland, where the fibrous root system is abundant and evenly distributed within the shallow soil (Wahren

et al., 2009; Alaoui et al., 2011). It will result in non-uniformly shallow infiltration if the fine roots are developed shallowly and the coarse roots are inclined but not deeply rooted. It is more common in areas with mixed grass and shrub growth or some trees (such as deciduous forests), where shallow fine roots develop and thick roots grow variably (Luo et al., 2019; Zuo et al., 2021). When the coarse roots are deeply rooted and the fine roots that accompany them are well developed, the result is deep infiltration. This occurs frequently in areas where large trees (such as forests) have a well-developed primary root system that generates excellent preferential flow channels in the deeper soil layers (Luo et al., 2019; Alaoui et al., 2011).

Of course, the soil in southwest China is not homogenous, the water can also flow from the soil matrix due to the existence of bigger pores around the root-soil system. We also discover undyed roots in the shallow layer, proving that not all roots are preferred water channels. Similar findings are reached by Luo et al. (2018), who find that specific existing roots do not help soil water transport. However, the majority of coarse roots are more undyed, and the smaller the diameter, the more dyed the roots are. This may be due to the distinct roles that coarse and fine roots play in water infiltration, as well as potential connections to the physiological properties of coarse and fine roots. The roots with smaller diameters are mostly absorbent roots, which are dyed during water flow as a result of water absorption by plant life activities (Wang et al., 2015; Zhao et al., 2014). Coarse roots, on the other hand, can only be dyed for a brief time by water infiltration.

#### 4.2. Root promotes water flow at the pore scale

The process of liquid surface lowering, which is also called the two-phase flow of water-driven air, is mainly influenced by the viscosity ratio, interfacial tension, wettability of the two-phase fluid, and the pore structure characteristics (Cejas et al., 2014; de Anna et al., 2020). In regular capillary tubes, the liquid surface always lowers along the side walls with smaller contact angles (Jang et al., 2016). But once within the pore, the particle morphology causes the flow route to growing narrower, which in turn causes the liquid surface velocity at the particle wall to increase and the liquid surface lowering. This illustrates the need to create pore throats to explore the change in the fluid surface under different conditions, as this can affect the overall flow path of water. Due to the contact angle and particle morphology limitations, the liquid surface lowers along the root wall.

The water potential conditions within the infiltration zone are the basic factors affecting the change in infiltration rate, and the rate of soil infiltration shows a decreasing trend with time (Bodman and Colman, 1944). The dyeing in shallow soil is more uniform in the dye experiment because the water flow in both the root-soil pores and soil pores is mainly influenced by the total potential gradient within the upper part of the wet soil (Fig. 7). While in deep soil layers, the fluid is primarily affected by gravity and capillary forces, the root serves as a conduit to move water from one pore to the next, whereas water between soil particles can only remain close to the pore throat. A preferential flow path similar to that in Fig. 9 eventually forms in the root-soil pore as a result of the roots.

From a single pore channel of the RP model, the rate of liquid surface flow along the root side of the root-soil pore is greater than that along the particle side (Fig. 8). The rate of liquid surface flow along the root wall of the root-soil pore is greater than that along the particle wall (Fig. 8). The root side liquid surface movement pulls the liquid surface downward, causing water to lower on the particle wall and even throughout the entire pore space. Additionally, it is found that soil porosity away from the root axis reduces with increasing distance and lowers with increasing  $d_r$  and root density utilizing CT scans (Helliwell et al., 2017; Helliwell et al., 2019). Therefore, even in the absence of pressure conditions, water is more likely to flow across the soil matrix along the root axis under the influence of gravity and capillary forces (Mair et al., 2022).

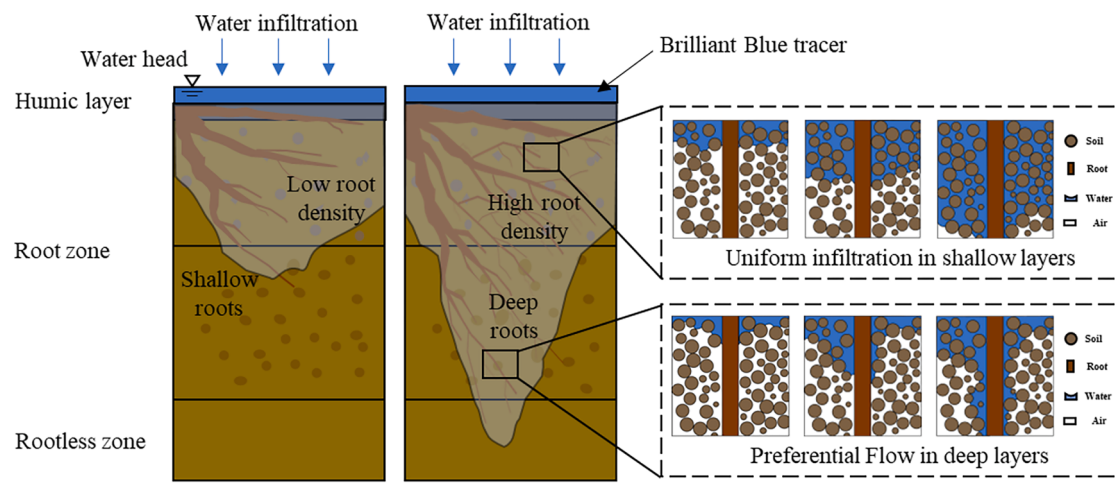


**Fig. 9.** Concept map of root-induced preferential flow.

The roots show various structural forms such as spongy or fibrous, resulting in roughness on the root surface (Hauber et al., 2020). According to the derivation of the Wenzel equation, it can be found that rough surfaces can increase the hydrophilicity of the hydrophilic materials for smooth surfaces (Wenzel, 1936). It also suggests that the simulated wall itself is hydrophilic and the actual root system has a rougher surface, which results in a smaller contact angle and easier fluid flow. Also, in the simulation, we assume that the fluid is water, but in reality, there are root secretions consisting of polysaccharides and small amounts of lipids around the root tip (Carminati et al., 2017; Read et al., 2003). Ahmed et al. (2016a) explored the contact angle of dry mucilage collected from maize plants and found that the contact angle decreased for lower mucilage concentrations. Therefore, the effect of root biochemistry on the inter-root fluid contact angle also needs to be considered in future investigations.

Moreover, the  $d_r$  determines the number of pores between root and soil particles in the cross-section. For a single root, the larger the diameter, the more soil particles come into touch with the root cross-section. The specific surface area of fine roots is larger than that of coarse roots at the same RAD because there are more fine roots than coarse roots. As a result, locations with a higher density of fine roots are more likely to increase water flow because they have fine roots in contact with more soil particles at the same RAD.

## 5. Conclusion

The water infiltration at the field scale and the pore scale are investigated to clarify why roots promote preferential water movement. The conclusions are as follows.

(1) Both fine and coarse roots promote water infiltration. The RAD of fine roots is strongly correlated with DC, while the number of coarse roots is more strongly correlated with DC. And the density of fine roots shows a significant positive correlation with the Pr-fr.

(2) We propose three infiltration patterns in the root-soil zone based on the root density and the depth obtained from the experiment. Grass and cultivated areas are more likely to develop uniformly shallow infiltration, whereas mixed grass and irrigation or shallow-rooted tree areas are more likely to form non-uniformly shallow infiltration, and tree areas are more likely to generate deep infiltration. In addition, the infiltration pattern can also be evaluated based on the results of the field root profile.

(3) On the pore scale, there is a small difference in infiltration capacity between the root-soil pore and interparticle pore under high-pressure difference, resulting in uniform infiltration in shallow soils. While in the deep soil layer, water flows more easily along the roots and

at a faster rate than the water flow within the soil pores, thus creating a preferential flow.

The present study can be considered an advancement in explaining the preferential flow of water induced by the root system from multi-scale aspects.

## CRediT authorship contribution statement

**Jiaying Li:** Conceptualization, Methodology, Investigation, Formal analysis, Writing – review & editing. **Peng Cui:** Conceptualization, Funding acquisition, Supervision. **Yanzhou Yin:** Conceptualization, Methodology, Formal analysis, Writing – review & editing.

## Declaration of Competing Interest

The authors declare that they have no known competing financial interests or personal relationships that could have appeared to influence the work reported in this paper.

## Data availability

Data will be made available on request.

## Acknowledgments

This study was funded by the Second Tibetan Plateau Scientific Expedition and Research (No. 2019QZKK0903-02), the Strategic Priority Research Program of Chinese Academy of Sciences (No. XDA23090303), the National Key Research and Development Program of China (2022YFC3002902).

## References

- Ahmed, M.A., Kroener, E., Benard, P., Zarebanadkouki, M., Kaestner, A., Carminati, A., 2016a. Drying of mucilage causes water repellency in the rhizosphere of maize: measurements and modelling. *Plant Soil.* 407, 161–171. <https://doi.org/10.1007/s11104-015-2749-1>.
- Ahmed, S., Klassen, T.N., Keyes, S., Daly, M., Jones, D.L., Mavrogordato, M., Sinclair, I., Roose, T., 2016b. Imaging the interaction of roots and phosphate fertiliser granules using 4D X-ray tomography. *Plant Soil.* 401, 125–134. <https://doi.org/10.1007/s11104-015-2425-5>.
- Alaoui, A., Caduff, U., Gerke, H., Weingartner, R., 2011. A preferential flow effects on infiltration and runoff in grassland and forest soils. *Vadose Zone J.* 10, 367–377. <https://doi.org/10.2136/vzj2010.0076>.
- Ali, G., Macrae, M., Walker, M., Laing, J., Lobb, D., 2018. Preferential flow in vertisolic soils with and without organic amendments. *Agr. Env. Lett.* 3 (1), 180018.

- Allaire, S.E., Roulier, S., Cessna, A.J., 2009. Quantifying preferential flow in soils: a review of different techniques. *J. Hydrol.* 378, 179–204. <https://doi.org/10.1016/j.jhydrol.2009.08.013>.
- Amy McNally NASA/GSFC/HSL (2018), FLDAS Noah Land Surface Model L4 Global Monthly 0.1 x 0.1 degree (MERRA-2 and CHIRPS), Greenbelt, MD, USA, Goddard Earth Sciences Data and Information Services Center (GES DISC), Accessed: [Data Access Date], 10.5067/5NHC22T9375G.
- Bai, F., He, X., Yang, X., Zhou, R., Wang, C., 2017. Three dimensional phase-field investigation of droplet formation in microfluidic flow focusing devices with experimental validation. *Int. J. Multiph. Flow* 93, 130–141.
- Baker, H.J., Hutchins, M.G., Miller, J.D., 2021. How robust is the evidence for beneficial hydrological effects of urban tree planting? *Hydrolog. Sci. J.* 66, 1306–1320. <https://doi.org/10.1080/02626667.2021.1922692>.
- Balzano, B., Tarantino, A., Ridley, A., 2019. Preliminary analysis on the impacts of the rhizosphere on occurrence of rainfall-induced shallow landslides. *Landslides* 16, 1885–1901. <https://doi.org/10.1007/s10346-019-01197-5>.
- Bargues Tobella, A., Reese, H., Almaw, A., Bayala, J., Malmer, A., Laudon, H., Ilstedt, U., 2014. The effect of trees on preferential flow and soil infiltrability in an agroforestry parkland in semiarid Burkina Faso. *Water Resour. Res.* 50, 3342–3354. <https://doi.org/10.1002/2013WR015197>.
- Bodman, G., Colman, E., 1944. Moisture and energy conditions during downward entry of water into soils1. *Soil Sci. Soc. Am. J.* 8, 116–122. <https://doi.org/10.2136/sssaj1944.0361599500080000C0021x>.
- Boedner, G., Leitner, D., Kaul, H.P., 2014. Coarse and fine root plants affect pore size distributions differently. *Plant Soil.* 380, 133–151. <https://doi.org/10.1007/s11104-014-2079-8>.
- Booltink, H.W.G., Bouma, J., 1991. Physical and morphological characterization of bypass flow in a well-structured clay soil. *Soil Sci. Soc. Am. J.* 55, 1249–1254. <https://doi.org/10.2136/sssaj1991.03615995005000050009x>.
- Bronick, C.J., Lal, R., 2005. Soil structure and management: a review. *Geoderma* 124, 3–22. <https://doi.org/10.1016/j.geoderma.2004.03.005>.
- Cahn, J., Hilliard, J., 1958. Free energy of a non-uniform system. I. interfacial free energy. *The J. Chem. Phys.* 28, 258–267. <https://doi.org/10.1063/1.1744102>.
- Carminati, A., Benard, P., Ahmed, M.A., Zarebanadkouki, M., 2017. Liquid bridges at the root-soil interface. *Plant Soil.* 417, 1–15. <https://doi.org/10.1007/s11104-017-3227-8>.
- Cejas, C.M., Wei, Y., Barrois, R., Fretigny, C., Durian, D.J., Dreyfus, R., 2014. Kinetics of gravity-driven water channels under steady rainfall. *Phys. Rev. E.* 90, 042205. <https://doi.org/10.1103/PhysRevE.90.042205>.
- Chen, H., Lee, C.F., 2003. A dynamic model for rainfall-induced landslides on natural slopes. *Geomorphology* 51, 269–288. [https://doi.org/10.1016/S0169-555X\(02\)00224-6](https://doi.org/10.1016/S0169-555X(02)00224-6).
- Cui, Z., Wu, G.-L., Huang, Z.e., Liu, Y.u., 2019. Fine roots determine soil infiltration potential than soil water content in semi-arid grassland soils. *J. Hydrol.* 578, 124023.
- Cui, Z., Huang, Z.e., Liu, Y.u., López-Vicente, M., Wu, G.-L., 2022. Natural compensation mechanism of soil water infiltration through decayed roots in semi-arid vegetation species. *Sci. Total Environ.* 819, 151985.
- Dai, L.Y., Zhang, Y.H., Liu, Y., Xie, L.M., Zhao, S.Q., Zhang, Z.M., 2021. Thick roots and less microaggregates improve hydrological connectivity. *Chemosphere* 266, 129008. <https://doi.org/10.1016/j.chemosphere.2020.129008>.
- de Anna, P., Pahlavan, A.A., Yawata, Y., Stocker, R., Juanes, R., 2020. Chemotaxis under flow disorder shapes microbial dispersion in porous media. *Nat. Phys.* 17, 68–73. <https://doi.org/10.1038/s41567-020-1002-x>.
- Devitt, D.A., Smith, S.D., 2002. Root channel macropores enhance downward movement of water in a Mojave Desert ecosystem. *J. Arid Environ.* 50, 99–108. <https://doi.org/10.1006/jare.2001.0853>.
- Erktan, A., Cécillon, L., Graf, F., Roumet, C., Legout, C., Rey, F., 2015. Increase in soil aggregate stability along a Mediterranean successional gradient in severely eroded gully bed ecosystems: combined effects of soil, root traits and plant community characteristics. *Plant Soil.* 398, 121–137. <https://doi.org/10.1007/s11104-015-2647-6>.
- Fagerlia, N.K., Stone, L.F., 2006. Physical, chemical, and biological changes in the rhizosphere and nutrient availability. *J. Plant Nutr.* 29, 1327–1356. <https://doi.org/10.1080/01904160600767682>.
- Fan, Y., Miguez-Macho, G., Jobbagy, E.G., Jackson, R.B., Otero-Casal, C., 2017. Hydrologic regulation of plant rooting depth. *Proc. Natl. Acad. Sci. U. S. A.* 114, 10572–10577. <https://doi.org/10.1073/pnas.1712381114>.
- Flury, M., Flühler, H., 1995. Tracer characteristics of brilliant blue FCF. *Soil Sci. Soc. Am. J.* 59, 22–27. <https://doi.org/10.2136/sssaj1995.03615995005900010003x>.
- Freer, R., 1991. Bio-engineering: the use of vegetation in civil engineering. *Constr. Build. Mater.* 5, 23–26. [https://doi.org/10.1016/0950-0618\(91\)90028-J](https://doi.org/10.1016/0950-0618(91)90028-J).
- Freschet, G.T., Roumet, C., Treseder, K., 2017. Sampling roots to capture plant and soil functions. *Funct. Ecol.* 31, 1506–1518. <https://doi.org/10.1111/1365-2435.12883>.
- Freschet, G.T., Roumet, C., Comas, L.H., Weemstra, M., Bengough, A.G., Rewald, B., Bardgett, R.D., De Deyn, G.B., Johnson, D., Klimesova, J., Lukac, M., McCormack, M.L., Meier, I.C., Pages, L., Poorter, H., Prieto, I., Wurzburger, N., Zadworny, M., Bagniewska-Zadworna, A., Blancaflor, E.B., Brunner, I., Gessler, A., Hobbie, S.E., Iversen, C.M., Mommer, L., Picon-Cochard, C., Postma, J.A., Rose, L., Ryser, P., Scherer-Lorenzen, M., Soudzilovskaia, N.A., Sun, T., Valverde-Barrantes, O.J., Weigelt, A., York, L.M., Stokes, A., 2021. Root traits as drivers of plant and ecosystem functioning: current understanding, pitfalls and future research needs. *New Phytol.* 232, 1123–1158. <https://doi.org/10.1111/nph.17072>.
- Galloway, A.F., Pedersen, M.J., Merry, B., Marcus, S.E., Blacker, J., Benning, L.G., Field, K.J., Knox, J.P., 2018. Xyloglucan is released by plants and promotes soil particle aggregation. *New Phytol.* 217, 1128–1136. <https://doi.org/10.1111/nph.14897>.
- Ghestem, M., Sidle, R.C., Stokes, A., 2011. The influence of plant root systems on subsurface flow: implications for slope stability. *Bioscience* 61, 869–879. <https://doi.org/10.1525/bio.2011.61.11.6>.
- Hao, H.-X., Wei, Y.-J., Cao, D.-n., Guo, Z.-l., Shi, Z.-H., 2020. Vegetation restoration and fine roots promote soil infiltrability in heavy-textured soils. *Soil Tillage Res.* 198, 104542.
- Hauber, F., Konrad, W., Roth-Nebelsick, A., 2020. Aerial roots of orchids: the velamen radicum as a porous material for efficient imbibition of water. *Appl. Phys. A.* 126. <https://doi.org/10.1007/s00339-020-04047-7>.
- Helliwell, J.R., Sturrock, C.J., Mairhofer, S., Craigon, J., Ashton, R.W., Miller, A.J., Whalley, W.R., Mooney, S.J., 2017. The emergent rhizosphere: imaging the development of the porous architecture at the root-soil interface. *Sci. Rep.* 7. <https://doi.org/10.1038/s41598-017-14904-w>.
- Helliwell, J.R., Sturrock, C.J., Miller, A.J., Whalley, W.R., Mooney, S.J., 2019. The role of plant species and soil condition in the structural development of the rhizosphere. *Plant Cell Environ.* 42, 1974–1986. <https://doi.org/10.1111/pce.13529>.
- Hendrickx, J., Flury, M., 2001. Uniform and Preferential Flow Mechanisms in the Vadose Zone. *Conceptual Models of Flow and Transport in the Fractured Vadose Zone. In: Uniform and Preferential Flow Mechanisms in the Vadose Zone*, pp. 149–187.
- Jacqmin, D., 1999. Calculation of two-phase navier-stokes flows using phase-field modeling. *J. Comput. Phys.* 155, 96–127. <https://doi.org/10.1006/jcph.1999.6332>.
- Jang, J.B., Sun, Z.H., Santamarina, J.C., 2016. Capillary pressure across a pore throat in the presence of surfactants. *Water Resour. Res.* 52, 9586–9599. <https://doi.org/10.1002/2015wr018499>.
- Jiang, Y.J., Mehtab, A., Su, L.J., Muhammad, U., Shamsher, S., Li, J.J., Mahfuzur, R., 2022. Effect of root orientation on the strength characteristics of loess in drained and undrained triaxial tests. *Eng. Geol.* 296, 106459.
- Jiang, X.-J., Zhu, X., Yuan, Z.-Q., Li, X.G., Liu, W., Zakari, S., 2021. Lateral flow between bald and vegetation patches induces the degradation of alpine meadow in Qinghai-Tibetan Plateau. *Sci. Total Environ.* 751, 142338.
- Lei, J., Xu, Z., Xin, F., Lu, T.J., 2021. Dynamics of capillary flow in an undulated tube. *Phys. Fluids.* 33 (5), 052109.
- Levia, D., Frost, E., 2003. A review and evaluation of stemflow literature in hydrologic and biogeochemical cycles in forested and agricultural ecosystems. *J. Hydrol.* 274, 1–29. [https://doi.org/10.1016/S0022-1694\(02\)00399-2](https://doi.org/10.1016/S0022-1694(02)00399-2).
- Liu, H.W., Feng, S., Ng, C.W.W., 2016a. Analytical analysis of hydraulic effect of vegetation on shallow slope stability with different root architectures. *Comput. Geotech.* 80, 115–120. <https://doi.org/10.1016/j.comgeo.2016.06.006>.
- Liu, Z., Yu, X., Wan, L., 2016b. Capillary rise method for the measurement of the contact angle of soils. *Acta Geotech.* 11, 21–35. <https://doi.org/10.1007/s11440-014-0352-x>.
- Löbmann, M.T., Geitner, C., Wellstein, C., Zerbe, S., 2020. The influence of herbaceous vegetation on slope stability – a review. *Earth-Sci. Rev.* 209, 103328.
- Lormand, C., Zellmer, G.F., Németh, K., Kilgour, G., Mead, S., Palmer, A.S., Sakamoto, N., Yurimoto, H., Moebis, A., 2018. Weka trainable segmentation plugin in imagej: a semi-automatic tool applied to crystal size distributions of microlites in volcanic rocks. *Microsc. Microanal.* 24, 667–675. <https://doi.org/10.1017/s143192718015428>.
- Lu, N., Browne, C., Amchin, D., Nunes, J., Datta, S., 2019. Controlling capillary fingering using pore size gradients in disordered media. *Phys Rev Fluids* 4. <https://doi.org/10.1103/PhysRevFluids.4.084303>.
- Lu, J., Zhang, Q.i., Werner, A.D., Li, Y., Jiang, S., Tan, Z., 2020. Root-induced changes of soil hydraulic properties – a review. *J. Hydrol.* 589, 125203.
- Luo, Z.T., Niu, J.Z., Zhang, L., Chen, X.W., Zhang, W., Xie, B.Y., Du, J., Zhu, Z.J., Wu, S.S., Li, X., 2018. Roots-enhanced preferential flows in deciduous and coniferous forest soils revealed by dual-tracer experiments. *J. Environ. Qual.* 48, 136–146. <https://doi.org/10.2134/jeq2018.03.0091>.
- Luo, Z., Niu, J., Xie, B., Zhang, L., Chen, X., Berndtsson, R., Du, J., Ao, J., Yang, L., Zhu, S., 2019. Influence of root distribution on preferential flow in deciduous and coniferous forest soils. *Forests* 10 (11), 986.
- Mair, A., Dupuy, L.X., Ptashnyk, M., 2022. Model for water infiltration in vegetated soil with preferential flow oriented by plant roots. *Plant Soil.* 478, 709–729. <https://doi.org/10.1007/s11104-022-05501-6>.
- Markart, G., Kohl, B., Sotier, B., Klebiner, K., Schauer, T., Bunza, G., Pirk, H., Stern, R., 2011. A simple code of practice for the assessment of surface runoff coefficients for alpine soil-vegetation units in torrential rain (Version 2.0), 10th ed. Centre for Forests, Natural Hazards and Landscape, Innsbruck.
- Martinez, P., Buurman, P., do Nascimento, D.L., Almqvist, V., Vidal-Torrado, P., 2021. Substantial changes in podzol morphology after tree-roots modify soil porosity and hydrology in a tropical coastal rainforest. *Plant Soil.* 463 (1-2), 77–95.
- Mehtab, A., Jiang, Y.-J., Su, L.-J., Shamsher, S., Li, J.-J., Mahfuzur, R., 2020. Scaling the roots mechanical reinforcement in plantation of Cunninghamia R. Br in Southwest China. *Forests* 12 (1), 33.
- Mulyono, A., Subardja, A., Ekasari, I., Lailati, M., Sudirja, R., Ningrum, W., 2018. The hydromechanics of vegetation for slope stabilization. *IOP Conference Series: Earth and Environmental Science.* 118, 012038.
- Newman, B., Wilcox, B., Graham, R., 2004. Snowmelt-driven macropore flow and soil saturation in a semiarid forest. *Hydrol. Process.* 18, 1035–1042. <https://doi.org/10.1002/hyp.5521>.
- Nobles, M.M., Wilding, L., Lin, H., 2010. Flow pathways of bromide and Brilliant Blue FCF tracers in caliche soils. *J. Hydrol.* 393, 114–122. <https://doi.org/10.1016/j.jhydrol.2010.03.014>.
- Noguchi, S., Tsuboyama, Y., Sidle, R.C., Hosoda, I., 1997. Spatially distributed morphological characteristics of macropores in forest soils of hitachi ohta

- experimental watershed Japan. *J. Forest Res.-jpn.* 2, 207–215. <https://doi.org/10.1007/bf02348317>.
- Paterson, E., Gebbing, T., Abel, C., Sim, A., Telfer, G., 2007. Rhizodeposition shapes rhizosphere microbial community structure in organic soil. *New Phytol.* 173, 600–610. <https://doi.org/10.1111/j.1469-8137.2006.01931.x>.
- Qian, T., Wang, X.-P., Sheng, P., 2005. Molecular hydrodynamics of the moving contact line in two-phase immiscible flows. *Commun. Comput. Phys.*, p. 1.
- Qin, R.S., Bhadeshia, H.K., 2010. Phase field method phase field method. *Mater. Sci. Tech.-lond.* 26 (7), 803–811.
- Read, D., Bengough, A., Gregory, P., Crawford, J., Robinson, D., Scrimgeour, C., Young, I., Zhang, K., Zhang, X., 2003. Plant roots release phospholipid surfactants that modify the physical and chemical properties of soil. *New Phytol.* 157, 315–326. <https://doi.org/10.1046/j.1469-8137.2003.00665.x>.
- Rifa, J., Petrula, L., Hala, M., Alhasan, Z., 2018. Assessment of empirical formulae for determining the hydraulic conductivity of glass beads. *J. Hydrol. Hydromech.* 66, 337–347. <https://doi.org/10.2478/johh-2018-0021>.
- Scanlan, C.A., 2009. Processes and effects of root-induced changes to soil hydraulic properties. The University of Western Australia, Perth, Ph.D. diss. School of Earth and Environment.
- Schwarzel, K., Ebermann, S., Schalling, N., 2012. Evidence of double-funneling effect of beech trees by visualization of flow pathways using dye tracer. *J. Hydrol.* 470–471, 184–192. <https://doi.org/10.1016/j.jhydrol.2012.08.048>.
- Sidle, R.C., Bogaard, T.A., 2016. Dynamic earth system and ecological controls of rainfall-initiated landslides. *Earth-Sci. Rev.* 159, 275–291. <https://doi.org/10.1016/j.earscirev.2016.05.013>.
- Sidle, R., Noguchi, S., Tsuboyama, Y., Laursen, K., 2001. A conceptual model of preferential flow systems in forested hillslopes: evidence of self-organization. *Hydro Process.* 15, 1675–1692. <https://doi.org/10.1002/hyp.233>.
- Singh, S.R., Prakash, A., Hazra, B., Sarmah, A., Garg, A., Zhu, H.-H., 2018. Stochastic modelling of relative water permeability in vegetative soils with implications on stability of bioengineered slope. *Stoch. Env. Res. Risk A.* 32 (12), 3541–3559.
- Smettem, 1986. Analysis of water flow from cylindrical macropores. *Soil Sci. Soc. Am. J.* 50, 1139–1142. <https://doi.org/10.2136/sssaj1986.03615995005000050009x>.
- Song, L., Li, J.H., Zhou, T., Fredlund, D.G., 2017. Experimental study on unsaturated hydraulic properties of vegetated soil. *Ecol. Eng.* 103, 207–216. <https://doi.org/10.1016/j.ecoleng.2017.04.013>.
- Stokes, A., Lucas, A., Jouneau, L., 2007. Plant biomechanical strategies in response to frequent disturbance: uprooting of *Phyllostachys nidularia* (Poaceae) growing on landslide-prone slopes in Sichuan, China. *Am. J. Bot.* 94 (7), 1129–1136.
- Tisdall, J., Oades, J., 2006. Organic matter and water-stable aggregates in soils. *J. Soil Sci.* 33, 141–163. <https://doi.org/10.1111/j.1365-2389.1982.tb01755.x>.
- USDA-NRCS (1997) National Soil Characterization Database. USDA-NRCS Soil Survey Division. [http://www.statlab.iastate.edu/soils/ssl/natch\\_data.html](http://www.statlab.iastate.edu/soils/ssl/natch_data.html).
- van Schaik, N.L.M.B., 2009. Spatial variability of infiltration patterns related to site characteristics in a semi-arid watershed. *Catena* 78, 36–47. <https://doi.org/10.1016/j.catena.2009.02.017>.
- Vannoppen, W., Vanmaercke, M., De Baets, S., Poesen, J., 2015. A review of the mechanical effects of plant roots on concentrated flow erosion rates. *Earth-Sci. Rev.* 150, 666–678. <https://doi.org/10.1016/j.earscirev.2015.08.011>.
- Wahren, A., Feger, K.-H., Schwarzel, K., Münch, A., 2009. Land-use effects on flood generation - considering soil hydraulic measurements in modelling. *Adv. Geosci.* 21, 99–107.
- Wang, F., Chen, H.S., Lian, J.J., Fu, Z.Y., Nie, Y.P., 2018. Preferential flow in different soil architectures of a small karst catchment. *Vadose Zone J.* 17, 1–10. <https://doi.org/10.2136/vzj2018.05.0107>.
- Wang, Y., Shao, M., Liu, Z., Zhang, C., 2015. Characteristics of dried soil layers under apple orchards of different ages and their applications in soil water managements on the loess plateau of China. *Pedosphere* 25, 546–554. [https://doi.org/10.1016/S1002-0160\(15\)30035-7](https://doi.org/10.1016/S1002-0160(15)30035-7).
- Weiler, M., Naef, F., 2003. An experimental tracer study of the role of macropores infiltration in grassland soils. *Hydro Process.* 17, 477–493. <https://doi.org/10.1002/hyp.1136>.
- Wenzel, R.N., 1936. Resistance of solid surfaces to wetting by water. *Trans. Faraday Soc.* 28 (8), 988–994.
- Wu, X., Dang, X., Meng, Z., Fu, D., Cong, W., Zhao, F., Guo, J., 2022. Mechanisms of grazing management impact on preferential water flow and infiltration patterns in a semi-arid grassland in northern China. *Sci. Total Environ.* 813, 152082.
- Wu, T., Iii, W., Swanston, D., 1979. Strength of tree roots and landslides on Prince of Wales Island. Alaska. *Can. Geotech. J.* 16, 19–33. <https://doi.org/10.1139/t79-003>.
- Xiao, J., Luo, Y., Niu, M., Wang, Q., Wu, J., Liu, X., Xu, J., 2019. Study of imbibition in various geometries using phase field method. *Capillarity* 2 (4), 57–65.
- Zhang, G., Cui, P., Gualtieri, C., Zhang, J., Ahmed Bazai, N., Zhang, Z., Wang, J., Tang, J., Chen, R., Lei, M., 2021. Stormflow generation in a humid forest watershed controlled by antecedent wetness and rainfall amounts. *J. Hydrol.* 603, 127107.
- Zhang, C., Liu, G.B., Xue, S., Zhang, C.S., 2012. Rhizosphere soil microbial properties on abandoned croplands in the Loess Plateau, China during vegetation succession. *Eur. J. Soil Biol.* 50, 127–136.
- Zhao, X.N., Wu, P.T., Gao, X.D., Tian, L., Li, H.C., 2014. Changes of soil hydraulic properties under early-stage natural vegetation recovering on the Loess Plateau of China. *Catena* 113, 386–391. <https://doi.org/10.1016/j.catena.2013.08.023>.
- Zuo, F., Li, X.-Y., Yang, X., Ma, Y., Fangzhong, S., Liao, Q.-W., Li, D.-S., Wang, Y., Wang, R.-D., 2021. Linking root traits and soil moisture redistribution under *Achnatherum splendens* using electrical resistivity tomography and dye experiments. *Geoderma* 386, 114908. <https://doi.org/10.1016/j.geoderma.2020.114908>.